

Dominant Role of Molybdenum in the Electrochemical Deposition of Biological Macromolecules on Metallic Surfaces

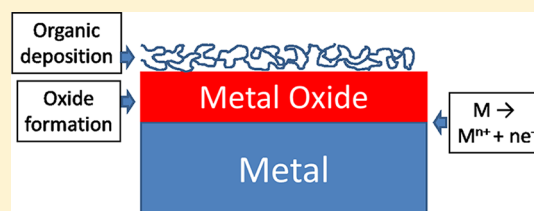
Elizabeth J. Martin,[†] Robin Pourzal,[†] Mathew T. Mathew,[‡] and Kenneth R. Shull^{*,†}

[†]Department of Materials Science and Engineering, Northwestern University, Evanston, Illinois 60208, United States

[‡]Department of Orthopedic Surgery, Section of Tribology, Rush University Medical Center, 1653 W. Congress Parkway, Chicago, Illinois 60612, United States

ABSTRACT: The corrosion of CoCrMo, an alloy frequently used in orthopedic implants, was studied with an electrochemical quartz crystal microbalance (QCM) in three physiologically relevant solutions. Mass changes were measured during potentiodynamic tests, showing material deposition in protein solutions at potential levels that caused mass loss when the proteins were not present. X-ray photoelectron spectroscopy (XPS) data indicated that the deposited material was primarily organic and therefore was most likely derived from proteins in the electrolyte.

Material deposition consistently occurred at a critical potential and was not dependent on the current density or total charge released into solution. Corrosion studies on pure Co, Cr, and Mo in protein solutions found material deposition only on Mo. We hypothesize that organic deposition results from the interaction of Mo(VI) with proteins in the surrounding solution. The organic layer is reminiscent of tribochemical reaction layers that form on the surface of CoCrMo hip bearings, suggesting that these types of layers can be formed by purely electrochemical means.



1. INTRODUCTION

Recently, serious concerns have been reported regarding the mechanical performance and safety of metal biomedical implants.^{1–4} Among the many factors that can affect implant performance, the corrosive nature of the physiological environment plays a significant role. Metal-on-metal (MoM) hip replacements, typically made of CoCrMo alloys, degrade because of the synergistic effects of mechanical wear from metal–metal contact and electrochemical reactions with salts, proteins, and other organic species.^{5,6} These degradative processes release metal ions and nanoscopic wear particles in vivo that often contribute to implant failure.^{7,8} However, studies have shown that a tribofilm, composed of organic and metallic constituents, can form under these same conditions on the surface of CoCrMo implants.⁸ Implants with such a tribofilm have demonstrated increased corrosion resistance; the film may also act as a lubrication layer, enabling better wear resistance.⁹ The organic constituents of this tribofilm are presumably derived from proteins in synovial fluid, but mechanisms causing the protein decomposition necessary for film formation are unknown. The current theory suggests that frictional processes contribute significantly to its development, with the combination of shear stresses and a rise in local contact temperatures causing protein degradation.⁸ Because it has been shown that tribofilms hold Co, Cr, and Mo ions,¹⁰ it is additionally hypothesized that local variations in corrosion kinetics involving proteins and metal ions contribute to the film formation.

In the study described here, we combined standard electrochemical techniques with a quartz crystal microbalance (QCM) mass sensor to delineate corrosion mechanisms of

CoCrMo and to investigate if tribofilm-like layers can be generated electrochemically. The QCM enables in situ quantification of surface changes accompanying corrosion and is very sensitive to small changes in the total mass of a thin film.^{11–15} Here, it was used to measure mass changes associated with the different sublayers of the alloy surface, including the metal, metal oxide, and any organic deposit, as depicted in the schematic in Figure 1. The instrument contains a thin piezoelectric quartz crystal set between two electrodes. When an oscillating voltage is applied across the electrodes, the quartz vibrates and its resonance frequency can be measured. If the mass on the electrode surface changes, so will the resonance frequency, providing detailed information that quantifies mass changes down to the nanogram level.¹⁶ The QCM is also

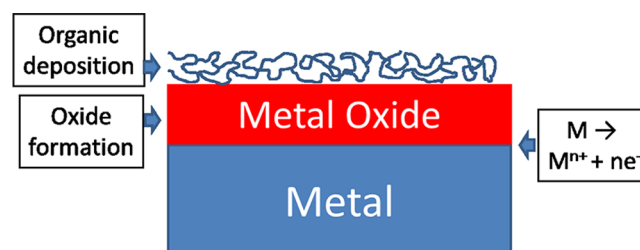


Figure 1. Schematic representation of a metal surface under oxidizing conditions in the presence of macromolecules that are able to form an organic deposit at the metal/solution interface.

Received: October 11, 2012

Revised: March 13, 2013

Published: April 3, 2013

sensitive to viscoelastic properties that introduce dissipation and reduce the quality factor of the resonance.¹⁷ Although a variety of equivalent measures can be used to quantify this dissipation, we use the half-width at half-maximum of the conductance peak centered at the resonance frequency. The use of this quantity, which we refer to as Γ , has been used extensively by others and is discussed in more detail in a review article by Johannsmann.¹⁸

The QCM has been used to study a variety of corrosion processes in different materials, including Fe–Cr and Au–Pd–In alloys.^{11–13} Recently, Valero Vidal et al.¹⁹ employed an electrochemical QCM to investigate passive film growth on CoCrMo films in phosphate-buffered saline (PBS). Mass loss was observed in all anodic potential ranges investigated, even during oxide growth, but was accelerated upon transpassive dissolution. In the present study, the corrosion behavior of CoCrMo thin films was measured in three different fluids that mimic different aspects of the physiological environment. Electrochemical QCM measurements were employed to quantify mass changes associated with the corrosion process. In potentiodynamic and potentiostatic tests indicated critical criteria for deposition of this organic layer. Additionally, similar corrosion tests were conducted on thin films of the individual alloying elements (Co, Cr, and Mo) to determine if a particular ion is responsible for the organic deposition. As we describe in the following sections, it was found that a significantly thick organic film formed on the Mo films, suggesting that Mo ions are essential to promoting organic film formation on the alloy.

2. EXPERIMENTAL METHODS

2.1. Sample Preparation. Working electrode specimens were prepared on AT-cut, 5 MHz quartz crystals with chrome electrodes (Inficon, East Syracuse, NY). CoCrMo, Cr, and Mo films were fabricated in a magnetron sputter deposition chamber (AJA Orion, N. Scituate, MA) at a base pressure of 10^{-7} Torr with Ar as the working gas. CoCrMo was deposited with a multistep sputter method modified from Nakagawa et al., which was designed to control the film's crystallinity and internal stresses.²⁰ First, the chamber was heated to 300 °C at a rate of 14 °C/min; crystals were then cleaned with a plasma strike. Subsequently, Cr was sputtered for 200 s at 100 W power and 3 mTorr pressure to produce an adhesion layer. Using a wrought, low-carbon CoCrMo target (ASTM F1537), a CoCrMo underlayer was deposited by sputtering for 100 s at 180 W power and 0.25 mTorr. Finally, CoCrMo was sputtered for 2000 s at 150 W power and 4 mTorr pressure. Cr films were made by sputtering at 300 °C and 3 mTorr pressure for 3000 s at 180 W power following the plasma cleaning step. Mo films were prepared at room temperature. Following the plasma strike, a Cr adhesion layer was deposited by sputtering for 200 s at 100 W power; Mo was then sputtered for 2000 s at 180 W power. Co films were prepared using an Edwards Auto 500 electron beam evaporator (BOC Edwards, Wilmington, MA) evacuated to a base pressure of 10^{-5} Torr. A Cr adhesion layer (5 nm thick) was first deposited at a rate of 0.08 nm/s at 40 mA beam current. Co (International Advanced Materials, Spring Valley, NY) was deposited at the same rate at 100 mA beam current to a thickness of between 130 and 300 nm. Low-carbon CoCrMo pins (ASTM F1537) with a diameter of 7 mm were utilized for bulk specimen tests. Prior to testing, pins were ground and polished with standard metallographic methods to a mirror finish ($R_a < 0.02 \mu\text{m}$).

2.2. Electrochemical QCM. Electrochemical tests were conducted in a custom three-electrode corrosion cell. The sputtered metal films on the quartz substrate acted as the working electrode, with an exposed area of 2.85 cm^2 . Two electrical leads connected the QCM holder to a QCM network analyzer and the potentiostat (BioLogic SP-

150, France), as shown schematically in Figure 2. Mammalian Ringer's salt solution (Electron Microscopy Services, Hatfield, PA), buffer

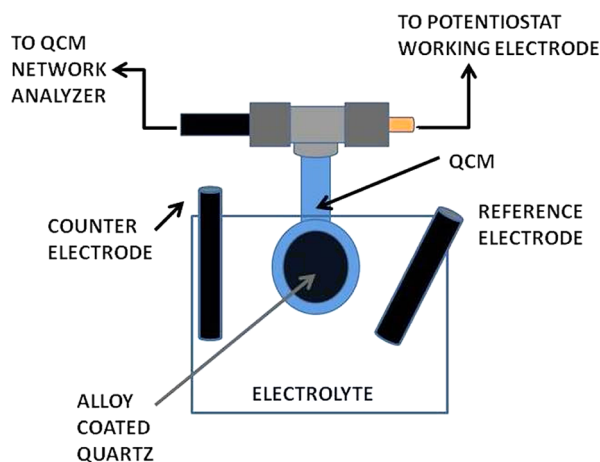


Figure 2. Schematic of the electrochemical QCM corrosion cell.

solution (pH 7.6), or bovine calf serum (BCS) served as the electrolyte. BCS is commonly used as a testing fluid for wear tests of orthopedic bearings. Its protein content is comparable to that of natural joint fluid (synovial fluid) with 30 g/L protein. Ringer's solution was used as manufactured and consisted of NaCl, KCl, MgCl_2 , CaCl_2 , NaHCO_3 , and glucose. Buffer solution was prepared with 0.154 M NaCl, 0.223 M Tris buffer, and 53.7 mM EDTA, adjusted to pH 7.6 with HCl. BCS was prepared by diluting newborn calf serum (Invitrogen, Grand Island, NY) in buffer solution.

Prior to each experiment, the open circuit potential was measured for 3 min by allowing the potential at the working electrode to equilibrate in the electrolyte. Next, the specimen was held at a cathodic potential of -0.9 V for 10 min to clean the surface and remove any oxide film that may have formed in air. The open circuit potential was then measured after the system was allowed to stabilize for 1 h. Subsequently, potentiodynamic and potentiostatic tests were conducted under varying conditions while the QCM frequency response was measured at the first, third, and fifth harmonics ($n = 1, 5 \text{ MHz}$; $n = 3, 15 \text{ MHz}$; $n = 5, 25 \text{ MHz}$). In many cases, QCM data from only the third harmonic are reported for clarity, but the data showed good agreement among all three harmonics. As discussed in more detail below, the experiments are generally conducted in the range where a simple analysis based on only a single harmonic is sufficient. During potentiodynamic tests, the potential was increased at a rate of 0.25 mV/s from -0.8 to 1.0 V . All potentials are reported against a saturated calomel reference electrode (SCE). The corrosion potential (E_{corr}) and current (i_{corr}) were extracted from the polarization curves by the Tafel method²¹ conducted with EC-Lab Express software. Tests were conducted at room temperature.

QCM frequency shifts were related to the mass change per unit area (ΔM_A) on the working electrode surface with the Sauerbrey equation²²

$$\Delta f_s = \frac{-2\eta f_1^2}{Z_q} \Delta M_A \quad (1)$$

where Z_q is the theoretical acoustic impedance of quartz ($8.84 \times 10^6 \text{ kg m}^{-2} \text{ s}^{-1}$), n is the order of the measured harmonic (1, 3, or 5), and f_1 is the fundamental frequency (5 MHz). The baseline frequency for a given harmonic corresponds to the resonance frequency of the crystal at the outset of a potentiometric scan after the system equilibrated for 1 h and the open circuit potential was measured. The Sauerbrey equation was originally applied to quartz resonators in air or vacuum, but it has been subsequently shown that the analysis can also be applied to mass deposition from a liquid medium. The analysis holds in a liquid medium provided that the reference frequency corresponds to the resonance frequency of the immersed crystal prior to the

deposition process and that the dissipation (Γ) due to viscoelastic effects is not very high.²³ The thickness of the metal film prior to testing was also extracted from eq 1 by measuring the resonance frequency before and after film deposition and by assuming that the sputtered density is the same as for the bulk material.

2.3. X-ray Photoelectron Spectroscopy and Energy-Dispersive Spectroscopy. X-ray photoelectron spectroscopy (XPS) was conducted with a Thermo Scientific ESCALAB 250Xi spectrometer (Thermo Fisher Scientific) using a monochromatized Al $K\alpha$ X-ray source at a 90° takeoff angle. The analysis spot size had a diameter of 500 μm . The base pressure in the analysis chamber was $\sim 10^{-9}$ mbar. Survey spectra (0–1100 eV) were obtained at a 100 eV analyzer pass energy with a 1.0 eV energy step size. High-resolution spectra of C 1s, O 1s, N 1s, Co 2p, Cr 2p, and Mo 3d were obtained at a 50 eV analyzer pass energy with a 0.5 eV energy step size. A flood gun was employed to control the surface potential throughout spectra acquisition. Peak fitting was conducted with Avantage software (Thermo Scientific) using a Shirley-type background and Gaussian/Lorentzian peak shapes. Binding energies were referenced by shifting the lowest-energy C 1s peak (hydrocarbon peak) to 284.8 eV. Analysis was performed on three areas for each sample. Five C 1s and O 1s and 10–20 N 1s, Co 2p, Cr 2p, and Mo 3d high-resolution scans were conducted for each area. Peak binding energies and atomic percentages are reported as an average \pm one standard deviation.

Energy-dispersive spectroscopy (EDS) was conducted with a Hitachi S-3400-NII scanning electron microscope equipped with an Oxford Incax-act SDD energy dispersive X-ray spectrometer. Analysis was performed at 15–20 keV with a 90 s acquisition time.

3. RESULTS AND DISCUSSION

3.1. Characterization of the CoCrMo Thin Film. QCM measurements indicated that sputtered CoCrMo films ranged in thickness from 200 to 300 nm. EDS confirmed that the chemical composition matched that of the bulk alloy, with approximately 66% Co, 28% Cr, and 6% Mo by weight. Crystallinity was confirmed with transmission electron microscopy (TEM) in another study²⁴ that showed the film to have longitudinal, nanocrystalline grains and a hexagonal close-packed (hcp) lattice. Although the microstructure differs from that of the bulk alloy, it is comparable to the deformed subsurface of MoM hip joints, which also exhibits a nanocrystalline hcp structure resulting from a strain-induced phase transformation.²⁵ To determine how the electrochemical behavior of the sputtered CoCrMo thin film compared to that of the bulk alloy, potentiodynamic tests were conducted on both specimens in a BCS electrolyte. As displayed in Figure 3, both materials exhibit similar electrochemical behavior, which is consistent with the reported literature data.^{19,26,27} E_{corr} and i_{corr} of the bulk sample were -0.463 V and 1.85×10^{-7} A/cm², respectively, and E_{corr} and i_{corr} of the thin films ranged from

-0.585 to -0.318 V and 3.79×10^{-8} to 1.82×10^{-7} A/cm², depending on the sample. The qualitative features of the potentiodynamic scan for the bulk material can be used to divide the response into the following regimes: (1) a cathodic regime below ~ -0.6 V in which the current is determined by the reduction of water or dissolved oxygen; (2) a passive regime, extending from ~ -0.2 to ~ 0.5 V, where the current is nearly independent of the applied potential, indicating the presence of a protective oxide; and (3) a transpassive regime above the breakdown potential at ~ 0.5 V. The current peak and subsequent stabilization from 0.65 to 0.8 V is typically attributed to the oxidation of Cr(III) to Cr(VI), although the electrochemical behavior in this potential regime is poorly understood.^{26–29}

The electrochemical behavior above 1 V could not be studied because the thin film was destroyed under this aggressive oxidizing condition. Overall, the electrochemical behavior is characteristic of behavior previously reported for CoCrMo alloys.²⁶ The similarity between the bulk and thin-film responses is taken as evidence that the thin films are an accurate model for studying corrosion processes in CoCrMo alloys. The additional information provided by the QCM experiments with the thin films allows us to better understand the processes occurring in the different potential regimes introduced above and is the focus of the remainder of this Article.

3.2. Mass Change Behavior During the Corrosion of CoCrMo Thin Films. Mass changes on CoCrMo films were measured in situ during potentiodynamic tests in Ringer's solution, buffer solution, and BCS; the results are displayed in Figure 4 with the potentiodynamic response. Mass changes as a function of total charge released, obtained by integrating the current over time, are displayed in Figure 5. According to Faraday's law, the amount of mass lost during a corrosion process should scale linearly with the charge.²¹ In our notation, we write Faraday's law in the following way²¹

$$\Delta M_A = -q_A m_q \quad (2)$$

where ΔM_A is the change in mass per unit area, q_A is the charge density in equivalents per unit area, and m_q is the molar mass per charge ratio. Our sign convention here is that the current is positive during corrosion processes leading to decreases in the mass. Note that q_A is obtained from the integrated charge by dividing by Faraday's constant (96 500 C/equiv). In situations where corrosion mechanisms are changing, the behavior cannot be characterized by a single value of m_q . In these cases, we specify an effective value of m_q from the slope of a plot of the mass change versus charge:

$$m_q^{\text{eff}} \equiv -\frac{d(\Delta M_A)}{dq_A} \quad (3)$$

Changes in m_q^{eff} indicate a change in corrosion mechanisms or in the valence state of the corroding species.

3.2.1. Ringer's Solution. In each electrolyte, specimens did not exhibit appreciable mass change below 0.4 V, although the current began to increase at 0.3 V. In Ringer's solution (Figure 4a), the alloy continuously lost mass as the potential increased above 0.4 V. Figure 5a illustrates that the alloy corroded with a constant value of 15 g/equiv for m_q^{eff} . This value is significantly lower than what would be expected from the ideal mass per charge ratio of the alloy, which can be determined from the following equation²¹

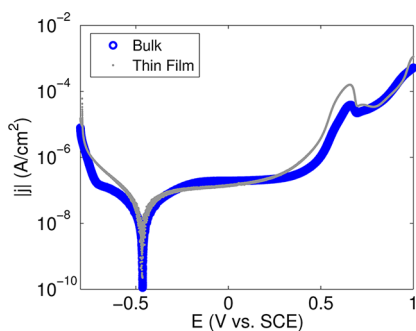


Figure 3. Comparison of electrochemical behavior of bulk and thin film CoCrMo. (Scan rate 0.25 mV/s.)

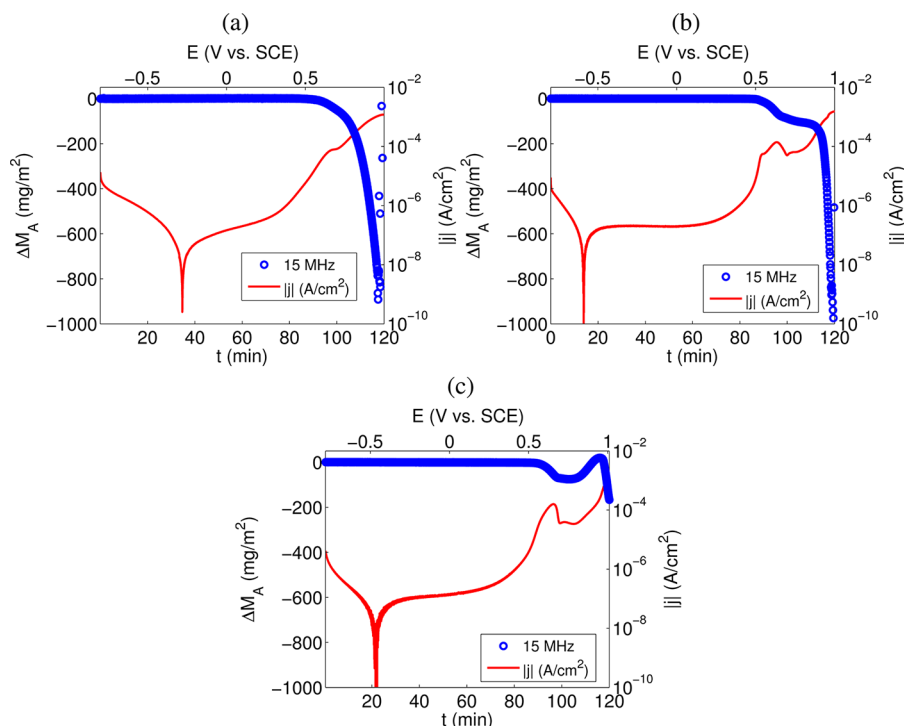


Figure 4. Mass changes and corresponding current density on CoCrMo thin films during potentiodynamic scans (scan rate: 0.25 mV/s) in (a) Ringer's solution, (b) buffer solution, and (c) BCS.

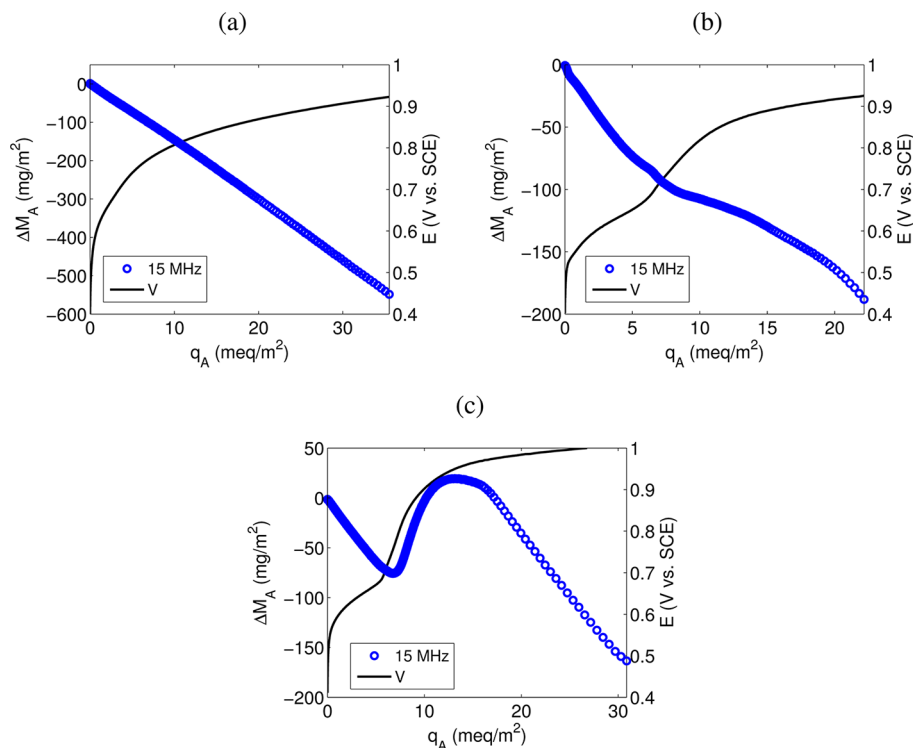


Figure 5. Change in mass on CoCrMo thin films as a function of charge released during potentiodynamic scans in (a) Ringer's solution, (b) buffer solution, and (c) BCS.

$$m_q = \left\{ \sum \frac{f_i n_i}{a_i} \right\}^{-1} \quad (4)$$

in which f_i , n_i , and a_i are the mass fraction, valence state, and molar mass of each alloying element, respectively. If the alloy is considered to have a composition of Co-29Cr-6Mo with

valence states of 2, 3, and 4 for the respective elements,²⁷ then a value of approximately 24 g/equiv is expected for m_q . In contrast, if the valence states of the corroding species are considered to be 2, 6 and 6, respectively, then the theoretical m_q ratio is 17, which is significantly closer to our measured value. The disagreement between the experimentally determined

value for m_q^{eff} and theoretically expected values for m_q likely results from the formation of an oxide film in solution, which grows while the alloy is simultaneously corroding. These results are consistent with what was reported by Valero Vidal et al.¹⁹ in PBS.

3.2.2. Buffer Solution. In buffer solution (Figures 4b and 5b), the film displayed a more distinct passive regime between -0.4 and 0.2 V but again began to lose mass at 0.4 V with $m_q^{\text{eff}} = 16$ g/equiv. In contrast to the experiment in Ringer's solution, the film that was corroded in buffer solution exhibited a current peak and subsequent stabilization between 0.65 and 0.8 V. Here, the rate of mass loss declined. As demonstrated in Figure 5b, m_q^{eff} dropped as low as 3.6 g/equiv between 0.75 and 0.85 V. Above 0.85 V, the rate of mass loss began to increase again with the current, approaching 18 g/equiv by the end of the potentiodynamic scan.

3.2.3. Bovine Calf Serum. As indicated in Figure 4c, the corrosion behavior in BCS was similar to that in buffer solution until the potential reached ~ 0.8 V. At this point, a substantial increase in the mass was observed, despite the increased current that predicts mass loss. Because the behavior was not seen in Ringer's or buffer solution and was not reported by Valero Vidal in PBS,¹⁹ mass gain presumably results from protein deposition. This deposited film persists to potentials up to about 0.93 V. At higher potentials, the underlying CoCrMo film corroded rapidly and was removed from the quartz crystal surface. The plot of mass change with charge (Figure 5c) shows that the alloy initially lost mass with an m_q^{eff} of 13 g/equiv. The rate of mass gain was not linear with charge, and the rate of final mass loss was not consistent among the samples.

3.2.4. Dissipation Measurements. Dissipation changes were also measured during potentiodynamic scans. In Ringer's and buffer solution, the dissipation remained relatively constant until the film began to lose mass. Neither the potential nor the degree of mass loss at which dissipation increased was consistent among the tests. In BCS, dissipation increased at approximately the same potential at which mass gain occurred. The ratio of the dissipation shift to frequency shift ($\Delta\Gamma/\Delta f$) from a potentiodynamic scan in BCS is shown in Figure 6.

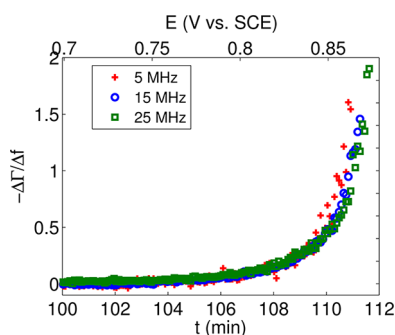


Figure 6. Ratio of dissipation to frequency shift on CoCrMo thin films during potentiodynamic scans in BCS. (Scan rate: 0.25 mV/s.)

Surface roughness can increase dissipation and cause an incorrectly large mass gain reading on the QCM if surface cavities entrap fluid.^{30–33} However, frequency shifts resulting from roughness for samples immersed in a liquid medium scale as $n^{1/2}$,³⁴ which was not true of our samples. The presence of a viscoelastic (rather than rigid) material on the QCM surface can also enhance dissipation. If viscoelastic effects are small, meaning $\Delta\Gamma/\Delta f \ll 1$, then eq 1 holds and Δf scales with the

harmonic order, n . If viscoelastic effects are significant, then ΔM_A as calculated from eq 1 will depend on the harmonic and a viscoelastic correction factor must be included in the analysis.^{18,35} In our experiments, as demonstrated in Figure 7, the value of ΔM_A obtained from the Sauerbrey equation was the same for all three harmonics prior to mass deposition and during the initial stages of the mass deposition process. Above ~ 0.85 V, $\Delta\Gamma/\Delta f$ became significant and ΔM_A became dependent on n . Hence, we attribute the enhanced dissipation to the viscoelastic character of this adsorbed layer, which supports the hypothesis that the measured mass increase in BCS results from protein deposition. Additional information about the viscoelastic properties of the deposited layer can be obtained from a more detailed analysis of Δf and $\Delta\Gamma$ in this highly dissipative regime.^{17,18,35} This analysis is the focus of an ongoing investigation.

3.3. Conditions for Mass Deposition on CoCrMo in BCS. To determine if there is a critical condition that promotes mass deposition on CoCrMo in BCS, the potential applied to the film was increased from -0.8 V and held constant at various levels. The current density, total charge (current integrated over time), and potential were quantified at the points at which the initial mass loss occurred, the rate of mass loss decreased, the mass increase began, and the final mass loss began. No clear correlation existed between these processes and the current density or integrated charge. However, the potentials at each point of mass change were consistent and are provided in Table 1. Mass deposition begins at potentials near 0.77 V in all cases, always following the current peak and stabilization that is characteristic of the transpassive regime. Thus, it is presumed that mass deposition results from reactions between proteins and the ionic species that are formed near this potential.

The data also indicate that there is a maximum potential for which the deposited film will remain stable for extended periods of time. When the potential was increased from -0.8 V at a rate of 0.25 mV/s and then held at 0.83 V, the film experienced comparable deposition as during the complete potentiodynamic scan but maintained the layer throughout the test, as displayed in Figure 8a,b. In contrast, when the potential was held near the end of the mass gain regime at 0.91 V (Figure 8c), the film corroded in nearly the same manner as when the potential was continuously increased to 1.0 V, even though the current density was comparable to that at 0.83 V (data not shown).

3.4. Individual Alloying Elements. Potentiodynamic tests were also conducted on the pure alloying elements in BCS to determine if a particular ion is responsible for mass deposition on the alloy. Mass changes with potential variation are shown for each metal in Figure 9. Cobalt specimens (Figure 9a) monotonically lost mass as the potential increased. Mass loss began near -0.48 V as the current reached a plateau. The m_q^{eff} (Figure 10a) averaged 29.3 ± 4.2 g/equiv, approximately corresponding to the Co(II) oxidation state as expected. Chromium specimens (Figure 9b) gained approximately 3.7 mg/m² mass at 0.38 V but continuously lost mass beginning at 0.5 V. The mass gain at 0.38 V is 1 to 2 orders of magnitude smaller than on the alloy and corresponds to a stabilization in the current. Hence, it is likely attributed to an enhancement in the oxide thickness on the chromium surface. The initial value of m_q^{eff} (Figure 10b) was approximately 9 g/equiv, nearly corresponding to the dissolution of Cr(VI) ions, but decreased to 6.7 g/equiv above 0.85 V.

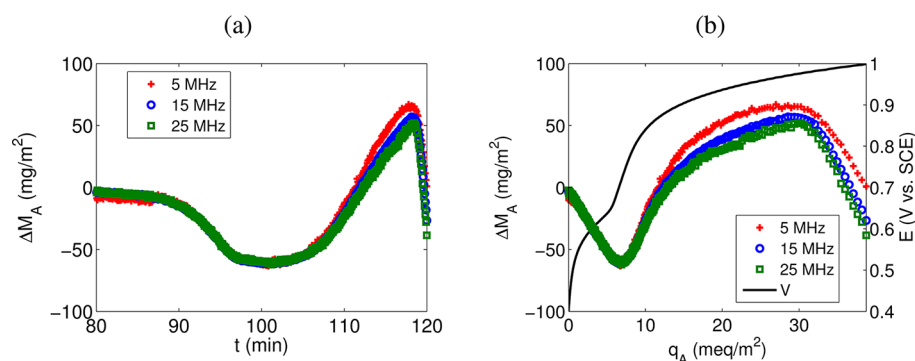


Figure 7. Mass changes on CoCrMo thin films during potentiodynamic scans in BCS, measured at three harmonics as a function of (a) potential and (b) released charge. (Scan rate: 0.25 mV/s.)

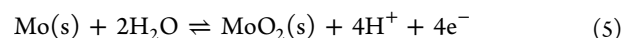
Table 1. Electrode Potential at Critical Points of Mass Change Behavior of CoCrMo Thin Films Corroded in BCS

	potential (V vs SCE)
initial mass loss	0.53 ± 0.04
mass stabilization	0.68 ± 0.02
mass increase	0.77 ± 0.04
final mass loss	0.92 ± 0.05

Molybdenum samples (Figure 9c) exhibited significantly different mass change behavior than cobalt or chromium. The metal film began to lose mass as the potential reached -0.16 ± 0.02 V with $m_q^{\text{eff}} = 15$ g/equiv (Figure 10c), corresponding to the dissolution of Mo(VI) ions. As the potential neared 0.06 ± 0.02 V or the current density reached approximately 5×10^{-4} A/cm², specimens gained at least 450 mg/m² mass. Some specimens gained nearly 5000 mg/m² mass. The QCM signal was lost at ~ 0.10 V because of the large frequency shift; therefore, tests were stopped at this potential. The mass did not

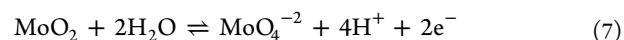
increase on Mo films during potentiodynamic tests in either Ringer's or buffer solution. Our hypothesis based on these results is that Mo(VI) ions are critical to the initiation of mass deposition on both the Mo and CoCrMo surfaces.

Neutral Mo oxidizes to Mo(IV), forming MoO₂ according to the following reaction with water above the potential E_0 :³⁶



$$E_0 = 0.313 - .0591\text{pH} \quad (6)$$

This reaction occurs spontaneously at all pH values relevant to our experiment, thus our assumption is that a thin layer of MoO₂ is always present at the metal surface. At higher potentials, Mo(IV) further oxidizes to Mo(VI) according to the following reaction:³⁶



The equilibrium reduction potential (vs SCE) for this reaction is³⁶

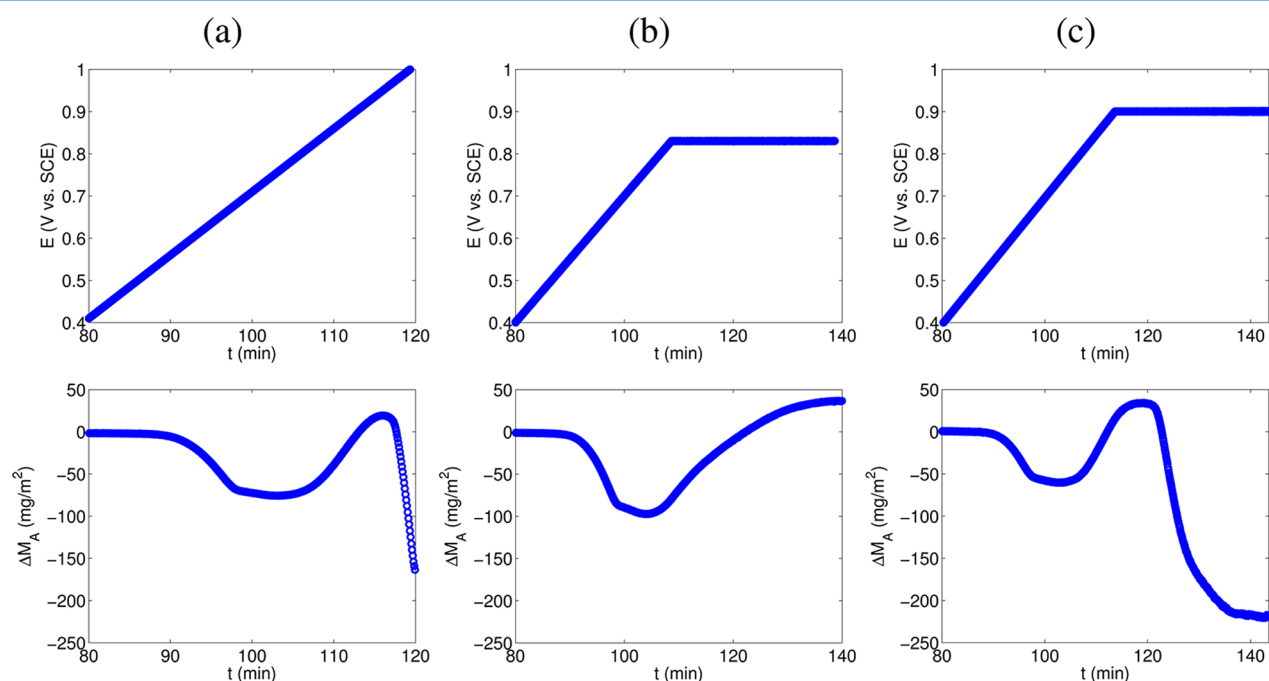


Figure 8. Time dependence of the potential applied to CoCrMo thin films (upper) and of the corresponding mass changes (lower) in experiments to determine the conditions promoting deposition in BCS solutions. (a) Potential ramped from -0.8 to 1.2 V. (b) Potential ramped from -0.8 to 0.83 V and held at 0.83 V. (c) Potential ramped from -0.8 to 0.91 V and held at 0.91 V.

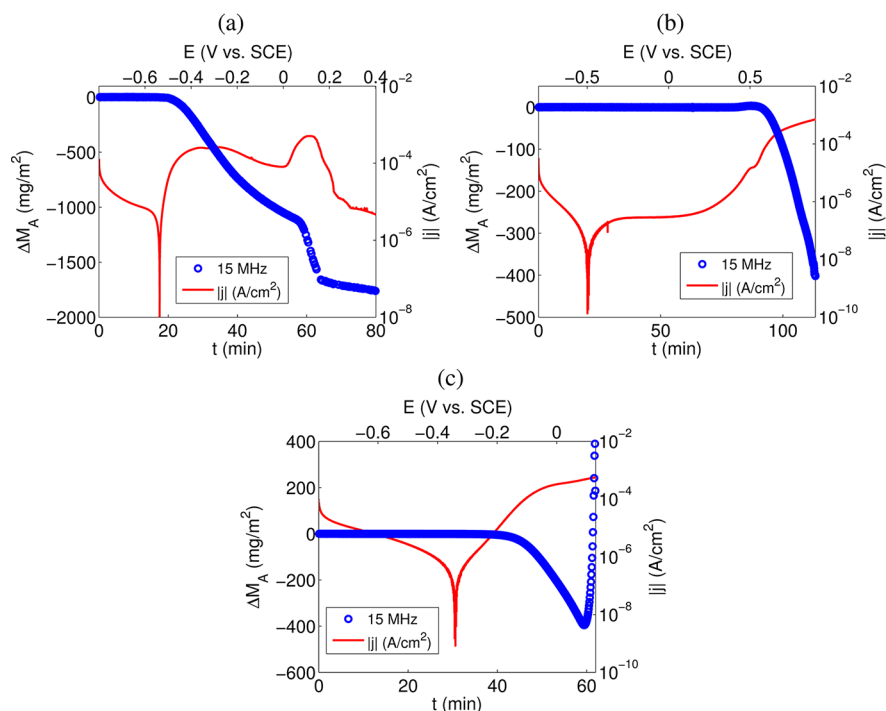


Figure 9. Mass changes and corresponding current density of (a) Co, (b) Cr, and (c) Mo thin films during potentiodynamic scans in BCS. (Scan rate: 0.25 mV/s.)

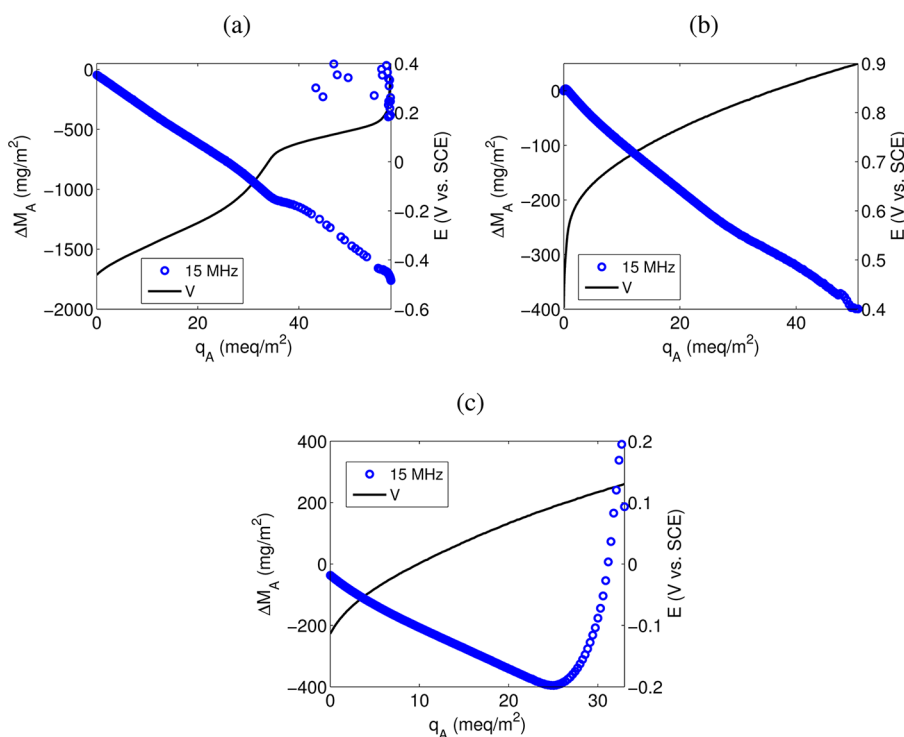


Figure 10. Change in mass as a function of charge released during potentiodynamic scans in BCS on (a) Co, (b) Cr, and (c) Mo thin films.

$$E_0 = 0.362 - 0.1182\text{pH} + 0.0295 \log[\text{MoO}_4^{-2}] \quad (8)$$

No other reaction is predicted until water is oxidized to evolve O_2 .³⁶

A useful estimate of the molybdate (MoO_4^{-2}) ion concentration at the point at which mass deposition occurs can be obtained by assuming that all of the mass loss up to this point is due to the release of Mo from the surface as MoO_4^{-2} .

From Figure 9c we see that mass deposition occurs when $\sim 400 \text{ mg/m}^2$ of Mo has been released into solution, corresponding to a surface molybdate concentration, $[\text{MoO}_4^{-2}]$, of $\sim 4 \times 10^{-3} \text{ mol/m}^2$. These ions are concentrated within a thin layer of width, $l \approx (Dt)^{1/2}$, where D is the diffusion coefficient of the ions in solution and t is the time that the ions have had to diffuse. For the molybdate ions, we expect $D \approx 3 \times 10^{-10} \text{ m}^2/\text{s}$, a value comparable to the diffusion coefficient of similarly sized

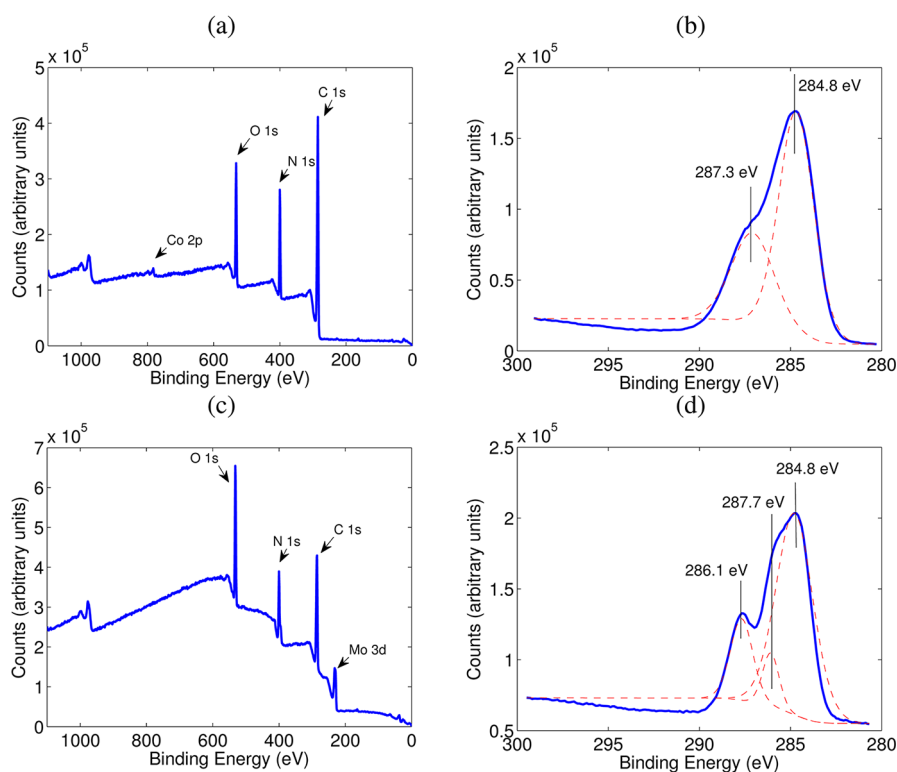


Figure 11. XPS survey scans and decomposed C 1s spectra of CoCrMo and Mo surfaces following mass deposition in BCS. (a) CoCrMo survey, (b) CoCrMo C 1s, (c) Mo survey, and (d) Mo C 1s.

ions in water.³⁷ Mass deposition occurs about 15 min after molybdate ions are first released in solution (Figure 9c). Taking $t = 900$ s, we obtain $l \approx 5 \times 10^{-4}$ m and $[\text{MoO}_4^{2-}]_s/l \approx 8$ mol/m³, corresponding to a molar concentration of 8×10^{-3} M.

The measured potential at which oxidation to Mo(VI) occurs is consistent with eq 8 provided that possible changes in the local pH are accounted for. For example, if we assume $[\text{MoO}_4^{2-}] = 8$ mM and a pH equal to the starting pH of the BCS solution (7.6), then we obtain $E_0 = -0.6$ V from eq 8. At the opposite extreme, we can assume that the BCS solution has no buffering capacity so that the eight protons released by the combination of the reactions shown in eqs 5 and 7 contribute to the decrease in the local pH. In this case, the pH is reduced to ~ 1 and we obtain $E_0 = 0.182$ V from eq 8. Not surprisingly, the measured potential range over which molybdate ions are released into solution is between these two extremes. Kinetic effects will also play a role here because the equilibrium conditions for which eq 8 can be applied quantitatively are not established under the corrosion conditions relevant to our experiments.

It is likely that any change in local pH that occurs upon oxidation of molybdenum will induce changes in the surface charge of the Mo specimen and proteins in solution, leading to mass deposition from electrostatic adsorption. However, the magnitude of mass increase measured by the QCM is significantly greater than what would result from a monolayer of adsorbed proteins. For example, Ithurbide et al. found that the adsorption of albumin onto a passivated chromium specimen increased the mass on the surface by only 4 mg/m², which is 2 to 3 orders of magnitude smaller than what was measured in this study.³⁸ Thus, whereas the local protein/substrate interactions may play an important role in the adhesion of the interfacial layer to the metallic substrate, the

measured mass gain cannot be explained by adsorption processes that by definition are confined to the immediate vicinity of the metallic surface. It is more appropriate to think of the mass gain as resulting from the formation of some sort of interfacial phase that forms upon the release of Mo(VI) ions (presumably in the form of molybdates) into a solution that contains appropriate macromolecules. On the CoCrMo alloy, the mass gain occurs at potentials within the secondary passive regime where the electrochemical behavior is believed to be controlled by the oxidation of Cr(III) to Cr(VI). However, because mass deposition occurred only on the Mo films and not on Co nor Cr, we conclude that a release of Mo(VI) ions rather than Cr(VI) is necessary to forming the deposit on the CoCrMo surface.

3.5. X-ray Photoelectron Spectroscopy. XPS was used to assess the composition of the deposited layers on QCM specimens that exhibited material deposition without subsequent mass loss. The CoCrMo specimen was prepared by conducting a potentiodynamic scan in BCS from -0.8 to 0.83 V at 0.25 mV/s and then holding the potential at 0.83 V for 30 min. The Mo sample was prepared by conducting a potentiodynamic scan in BCS from -0.8 to 0.08 V. Subsequently, specimens were rinsed once in deionized water and twice in methanol and dried with a compressed air canister to remove any serum that may have simply adhered to the film. A typical survey scan of each surface is shown in Figure 11. The peak binding energy and atomic percentage of each element is included in Table 2. Data confirm that the deposited layer on both metals is primarily organic and derived from proteins: the N 1s peak near 400 eV corresponds to the binding energy of amine or amide bonds, and the N to total C ratio (0.22 ± 0.02 on CoCrMo, 0.23 ± 0.07 on Mo) is the same as that reported for bovine serum albumin powder.³⁸ Additionally, the

Table 2. Binding Energies and Atomic Percentages of Elements Present on CoCrMo and Mo Surfaces after Mass Gain in BCS

	CoCrMo		Mo	
	peak BE (eV)	atom %	peak BE (eV)	atom %
C 1s	285.4 ± 0.1	74.2 ± 5.6	285.8 ± 0.02	60.9 ± 2.1
N 1s	399.8 ± 0.2	16.5 ± 0.03	400.0 ± 0.01	14.1 ± 4.1
O 1s	532.2 ± 0.02	8.8 ± 5.1	531.7 ± 0.1	23.2 ± 1.8
Co 2p	782.8 ± 0.5	0.27 ± 0.27		
Cr 2p				
Mo 3d			230.0 ± 0.2	4.3 ± 1.4

decomposition of the C 1s peak (Figure 11b,d) shows evidence of carbon in an organic binding environment. For CoCrMo, the C 1s peak was decomposed into two peaks; the peak at 284.8 ± 0.03 eV corresponds to adventitious carbon, and the peak at 287.3 ± 0.34 eV corresponds to carbon in an amine or amide bond.³⁹ The C 1s peak on the Mo specimen was decomposed into three peaks. In addition to the adventitious carbon peak, a peak is present at 286.1 ± 0.06 eV, attributed to C–O and C–N bonds,^{38,40} and at 287.7 ± 0.06 eV, attributed to peptide bonds.⁴¹ Neither specimen exhibited an appreciable metallic contribution. High-resolution scans at Cr 2p (570–595 eV) and Mo 3d (220–240 eV) on the CoCrMo specimen did not detect either element. Our primary conclusion from these results is that the deposited layer is primarily organic, with a very small metallic component.

4. SUMMARY

An electrochemical quartz crystal microbalance was utilized to investigate the corrosion of CoCrMo thin films in Ringer's solution, buffer solution, and bovine calf serum. Films were prepared in a manner such that their microstructure and electrochemical behavior model those of MoM hip joint surfaces. The key findings emerging from this work are as follows: (1) If proteins are present in solution, then the QCM measures a mass increase on the alloy surface during corrosion at elevated potentials. (2) Typical values for the mass of the deposited film range from 50 to 200 mg/m². (3) Material is deposited at a critical potential, 0.77 V, and can be maintained for some time at slightly higher potentials, suggesting that deposition results from redox reactions between oxidized alloying elements and proteins in solution. (4) Dissipation of the QCM signal increases with mass gain, providing evidence of a viscoelastic layer. (5) QCM measurements at multiple harmonics scale with the Sauerbrey equation prior to large increases in dissipation, indicating that mass gain measurements are real and not an artifact of roughness effects. (6) During the corrosion of Co, Cr, and Mo films in protein solutions, mass deposition was found only on the Mo films under conditions corresponding to the release of Mo(VI) ions into solution. From this, we infer that the mass gain results from interactions between Mo(VI) ions and proteins in solution. (7) XPS analysis of CoCrMo and Mo films after mass gain reveals a primarily organic surface, further supporting conclusions that mass gain results from protein deposition.

The organic film is reminiscent of tribochemical reaction layers that form on the surface of MoM hip bearings, suggesting the existence of local electrochemical pathways that promote the protein degradation essential for their formation. Because of the reproducibility of the experiments, these purely electrochemical experiments are very well suited for fundamental

investigations of tribochemical processes that also involve mechanical forces. Further investigations are being undertaken in order to more completely understand the mechanisms involved in the formation of these electrochemically induced organic reaction layers in vivo and their effects on the tribological performance of CoCrMo alloys.

AUTHOR INFORMATION

Notes

The authors declare no competing financial interest.

ACKNOWLEDGMENTS

This work was funded by the National Institutes of Health (NIH grant RC2 AR058993-01) and by the National Science Foundation (grant CMMI-0900586). XPS was performed at the NUANCE facility at Northwestern University, which is supported by the NSF, NSEC, NSF-MRSEC, Keck Foundation, and State of Illinois. We also thank Dr. Shilpi Vajpayee for her extensive work to establish the method of CoCrMo deposition and Christopher Nagelli for his assistance with the experimental setup.

REFERENCES

- (1) Smith, A. J.; Dieppe, P.; Vernon, K.; Porter, M.; Blom, A. W. Failure rates of stemmed metal-on-metal hip replacements: analysis of data from the national joint registry of England and Wales. *Lancet* **2012**, 379, 1199–1204.
- (2) Bernthal, N. M.; Celestre, P. C.; Stavrakis, A. I.; Ludington, J. C.; Oakes, D. A. Disappointing short-term results with the DePuy ASR XL metal-on-metal total hip arthroplasty. *J. Arthroplasty* **2012**, 27, 539–544.
- (3) Pelclova, D.; Sklensky, M.; Janicek, P.; Lach, K. Severe cobalt intoxication following hip replacement revision: clinical features and outcome. *Clin. Toxicol.* **2012**, 50, 262–265.
- (4) Pansard, E.; Fouilleron, N.; Deredre, G.; Migaud, H.; Girard, J. Severe corrosion after malpositioning of a metallic head over the Morse taper of a cementless hip arthroplasty. a case report. *Orthop. Traumatol.: Surg. Res.* **2012**, 98, 247–250.
- (5) Virtanen, S.; Milošev, I.; Gomez-Barrena, E.; Trebše, R.; Salo, J.; Kontinen, Y. Special modes of corrosion under physiological and simulated physiological conditions. *Acta Biomater.* **2008**, 4, 468–476.
- (6) Doorn, P. F.; Campbell, P. A.; Worrall, J.; Benya, P. D.; McKellop, H. A.; Amstutz, H. C. Metal wear particle characterization from metal on metal total hip replacements: Transmission electron microscopy study of periprosthetic tissues and isolated particles. *J. Biomed. Mater. Res.* **1998**, 42, 103–111.
- (7) Bozic, K. J.; Kurtz, S. M.; Lau, E.; Ong, K.; Vail, T. P.; Berry, D. J. The epidemiology of revision total hip arthroplasty in the united states. *J. Bone Joint Surg.* **2009**, 91, 128–133.
- (8) Wimmer, M. A.; Fischer, A.; Buscher, R.; Pourzal, R.; Sprecher, C.; Hauert, R.; Jacobs, J. J. Wear mechanisms in metal-on-metal bearings: the importance of tribochemical reaction layers. *J. Orthop. Res.* **2009**, 28, 436–443.
- (9) Liao, Y.; Pourzal, R.; Wimmer, M. A.; Jacobs, J. J.; Fischer, A.; Marks, L. D. Graphitic tribological layers in metal-on-metal hip replacements. *Science* **2011**, 334, 1687–1690.
- (10) Milošev, I.; Remškar, M. In vivo production of nanosized metal wear debris formed by tribochemical reaction as confirmed by high-resolution TEM and XPS analyses. *J. Biomed. Mater. Res., Part A* **2009**, 91, 1100–1110.
- (11) Buttry, D. A.; Ward, M. D. Measurement of interfacial processes at electrode surfaces with the electrochemical quartz crystal microbalance. *Chem. Rev.* **1992**, 92, 1355–1379.
- (12) Schmutz, P.; Landolt, D. In-situ microgravimetric studies of passive alloys: potential sweep and potential step experiments with fe-

25Cr and Fe-17Cr-33Mo in acid and alkaline solution. *Corros. Sci.* **1999**, *41*, 2143–2163.

(13) Leinartas, K.; Miecinkas, P.; Sudavicius, A.; Jelinskiene, D.; Juskenas, R.; Lisauskas, V.; Vengalis, B.; Juzeliunas, E. Corrosion of aU-Pd alloy in simulated physiological solutions. *J. Appl. Electrochem.* **2001**, *31*, 1079–1087.

(14) Olsson, C.-O. A.; Landolt, D. Film growth during anodic polarization in the passive region on 304 stainless steels with Cr, Mo, or W additions studied with EQCM and XPS. *J. Electrochem. Soc.* **2001**, *148*, B438.

(15) Hillman, A. The Electrochemical Quartz Crystal Microbalance. In *Encyclopedia of Electrochemistry*; Bard, A. J., Stratmann, M., Unwin, P. R., Eds.; Wiley-VCH: Weinheim, Germany, 2003; Vol. 3, pp 230–289.

(16) Brass, D. A.; Shull, K. R. Membrane-enhanced surface acoustic wave analysis of grafted polymer brushes. *J. Appl. Phys.* **2008**, *103*, 073517.

(17) DeNolf, G. C.; Haack, L.; Holubka, J.; Straccia, A.; Blohowiak, K.; Broadbent, C.; Shull, K. R. High frequency rheometry of viscoelastic coatings with the quartz crystal microbalance. *Langmuir* **2011**, *27*, 9873–9879.

(18) Johannsmann, D. Viscoelastic, mechanical, and dielectric measurements on complex samples with the quartz crystal microbalance. *Phys. Chem. Chem. Phys.* **2008**, *10*, 4516–4534.

(19) Valero Vidal, C.; Igual Munoz, A.; Olsson, C.-O. A.; Mischler, S. Passivation of a CoCrMo PVD alloy with biomedical composition under simulated physiological conditions studied by EQCM and XPS. *J. Electrochem. Soc.* **2012**, *159*, C233–C243.

(20) Nakagawa, S.; Akiyama, S.; Naoe, M. Methods to control internal stress in Co-Cr sputtered films on polymer tape for curl-free recording tape. *J. Magn. Magn. Mater.* **1994**, *134*, 354–361.

(21) Jones, D. *Principles and Prevention of Corrosion*, 2nd ed.; Prentice-Hall: Upper Saddle River, NJ, 1996.

(22) Sauerbrey, G. Verwendung von schwingquarzen zur wägung dünner schichten und zur mikrowägung. *Z. Phys. A* **1959**, *155*, 206–222.

(23) Martin, S. J.; Granstaff, V. E.; Frye, G. C. Characterization of a quartz crystal microbalance with simultaneous mass and liquid loading. *Anal. Chem.* **1991**, *63*, 2272–2281.

(24) Pourzal, R.; Martin, E. J.; Mathew, M. T.; Shull, K. R.; Tribological response of electrochemical corrosion layers on CoCrMo alloys *Tribol. Int.*, to be submitted for publication.

(25) Büscher, R.; Fischer, A. The pathways of dynamic recrystallization in all-metal hip joints. *Wear* **2005**, *259*, 887–897.

(26) Ouerd, A.; Alemanydumont, C.; Normand, B.; Szunerits, S. Reactivity of CoCrMo alloy in physiological medium: electrochemical characterization of the metal/protein interface. *Electrochim. Acta* **2008**, *53*, 4461–4469.

(27) Hodgson, A.; Kurz, S.; Virtanen, S.; Olsson, C.-O.; Mischler, S. Passive and transpassive behaviour of CoCrMo in simulated biological solutions. *Electrochim. Acta* **2004**, *49*, 2167–2178.

(28) Milošev, I.; Strehblow, H.-H. The composition of the surface passive film formed on CoCrMo alloy in simulated physiological solution. *Electrochim. Acta* **2003**, *48*, 2767–2774.

(29) Schmuki, P.; Virtanen, S.; Davenport, A. J.; Vitus, C. M. Transpassive dissolution of Cr and sputter-deposited Cr oxides studied by in situ X-ray near-edge spectroscopy. *J. Electrochem. Soc.* **1996**, *143*, 3997.

(30) Schumacher, R.; Gordon, J.; Melroy, O. Observation of morphological relaxation of copper and silver electrodes in solution using a quartz microbalance. *J. Electroanal. Chem. Interfacial Electrochem.* **1987**, *216*, 127–135.

(31) Yang, M.; Thompson, M.; Duncan-Hewitt, W. C. Interfacial properties and the response of the thickness-shear-mode acoustic wave sensor in liquids. *Langmuir* **1993**, *9*, 802–811.

(32) Yang, M.; Thompson, M. Surface morphology and the response of the thickness-shear mode acoustic wave sensor in liquids. *Langmuir* **1993**, *9*, 1990–1994.

(33) Daikhin, L.; Urbakh, M. Influence of surface roughness on the quartz crystal microbalance response in a solution new configuration for QCM studies. *Faraday Discuss.* **1997**, *107*, 27–38.

(34) Cho, N.-J.; D'Amour, J. N.; Stalgren, J.; Knoll, W.; Kanazawa, K.; Frank, C. W. Quartz resonator signatures under newtonian liquid loading for initial instrument check. *J. Colloid Interface Sci.* **2007**, *315*, 248–254.

(35) Johannsmann, D. Studies of Viscoelasticity with the QCM. In *Piezoelectric Sensors*, Steinem, C.; Janshoff, A., Eds.; Springer: Berlin, 2007; Vol. 5, pp 49–109.

(36) Pourbaix, M. *Atlas of Electrochemical Equilibria in Aqueous Solutions*; Pergamon Press: Oxford, 1996.

(37) Österlund, H.; Chlot, S.; Faarinen, M.; Widerlund, A.; Rodushkin, I.; Ingri, J.; Baxter, D. C. Simultaneous measurements of As, Mo, Sb, V and W using a ferrihydrite diffusive gradients in thin films (DGT) device. *Anal. Chim. Acta* **2010**, *682*, 59–65.

(38) Ithurbide, A.; Frateur, I.; Galtayries, A.; Marcus, P. XPS and flow-cell EQCM study of albumin adsorption on passivated chromium surfaces: influence of potential and pH. *Electrochim. Acta* **2007**, *53*, 1336–1345.

(39) Gruian, C.; Vanea, E.; Simon, S.; Simon, V. FTIR and XPS studies of protein adsorption onto functionalized bioactive glass. *Biochim. Biophys. Acta* **2012**, *1824*, 873–881.

(40) Tidwell, C. D.; Castner, D. G.; Golledge, S. L.; Ratner, B. D.; Meyer, K.; Hagenhoff, B.; Benninghoven, A. Static time-of-flight secondary ion mass spectrometry and X-ray photoelectron spectroscopy characterization of adsorbed albumin and fibronectin films. *Surf. Interface Anal.* **2001**, *31*, 724–733.

(41) Azioune, A.; Siroti, F.; Tanguy, J.; Jouini, M.; Chehimi, M. M.; Miksa, B.; Slomkowski, S. Interactions and conformational changes of human serum albumin at the surface of electrochemically synthesized thin polypyrrole films. *Electrochim. Acta* **2005**, *50*, 1661–1667.